Journal of Computational Physics **153,** 51–81 (1999)
Article ID jcph.1999.6274, available online at http://www.idealibrary.com on IDEAL®

Numerical Modeling of Magnetohydrodynamic Convection in a Rapidly Rotating Spherical Shell: Weak and Strong Field Dynamo Action

Weijia Kuang*,[1] and Jeremy Bloxham†

*Space Geodesy Branch, Code 926, NASA's Goddard Space Flight Center, Greenbelt, Maryland 20771; and †Department of Earth and Planetary Sciences, Harvard University, 20 Oxford street, Cambridge, Massachusetts 02138
E-mail: kuang@santafe.gsfc.nasa.gov

Received January 21, 1997; revised March 30, 1999

In this paper we describe a numerical model for investigating magnetohydrodynamic (MHD) convective flow of a Boussinesq fluid in a rapidly rotating spherical shell, driven by the buoyancy forces arising from incoming buoyant flux at the inner core boundary. The model is designed to investigate the generation of magnetic field in the Earth's fluid outer core. Our model differs from that of G. A. Glatzmaier and P. H. Roberts, who have recently investigated this problem, in several aspects. We apply a different physical approximation in the force balance of the system: instead of viscous stress, we use an axisymmetric inertial force to balance the axial magnetic torque arising from the Lorentz force; we use a mixed spectral–finite difference algorithm for better parallelization of the code; and apply different boundary conditions. We describe our numerical model in detail, and we test it by examining purely thermal convection in a rapidly rotating fluid shell and by examining Kumar–Roberts kinematic dynamos (modified for the spherical shell). Our results agree well with those of the previous studies. We also present a weak-field dynamo solution in a very simplified system and strong-field dynamo solutions in a more realistic system.

Key Words: rotating fluid; convection; magnetohydrodynamics; geomagnetism; dynamo processes.

[1]Also at Joint Center for Earth Systems Technology, University of Maryland, Baltimore County, 1000 Hilltop Circle, Baltimore, MD 21250.

0021-9991/99 $30.00

1. INTRODUCTION

Planetary magnetic fields are widely believed to be generated and maintained by convective flow in the interior regions of the planets, resulting in so-called dynamo action. In the case of the Earth, dynamo action is believed to occur in the iron-rich, fluid outer core.

The physics of dynamo action can be qualitatively described as follows: an electrically conducting fluid with a velocity $\mathbf{v}$ in a magnetic field $\mathbf{B}$ results in a current density $\mathbf{J}$ which, in the low-frequency magnetohydrodynamic (MHD) approximation, is given by

$$\mathbf{J} \equiv \frac{1}{\mu_0} \nabla \times \mathbf{B}, \tag{1.1}$$

where μ_0 is the magnetic permeability. This current modifies the flow $\mathbf{v}$ through the Lorentz force $\mathbf{F}_B$,

$$\mathbf{F}_B \equiv \mathbf{J} \times \mathbf{B}.$$

Dynamo action results if the magnetic field $\mathbf{B}$ is maintained against Ohmic decay.

In a rapidly rotating system, the flow is strongly influenced by the Coriolis force $\mathbf{F}_\Omega$ which, in the co-rotating reference frame, is given by

$$\mathbf{F}_\Omega \equiv 2\rho \boldsymbol{\Omega} \times \mathbf{v},$$

where ρ is the fluid density and $\boldsymbol{\Omega}$ is the angular velocity of the system. Dynamos may be categorized into weak-field dynamos in which $\mathbf{F}_B \ll \mathbf{F}_\Omega$, and strong-field dynamos in which $\mathbf{F}_B \sim \mathbf{F}_\Omega$.

Magneto-convection studies [6] show that the Coriolis force and the Lorentz force, if acting alone, help stabilize the system against buoyancy forces. When both forces act on the system and are similar in magnitude, the stabilizing effects of the forces offset each other and the system becomes most unstable. The Earth's dynamo (the geodynamo) is believed to be a strong-field dynamo.

Despite much study, the details of this process are poorly understood, in part because dynamo solutions must necessarily be three-dimensional [7], and because the Coriolis force $\mathbf{F}_\Omega$ makes the already complicated nonlinear governing equations even more difficult to solve numerically, as we shall demonstrate in the following sections.

Hindered by the difficulties, most previous studies have focused on simplified systems, such as generation of a magnetic field with a prescribed flow (the kinematic dynamo problem) or systems incorporating a parameterization of the nonlinear interactions (such as the $\alpha\omega$-dynamo problem). For a more detailed review, see, e.g., Gubbins and Roberts [8].

With the rapid development in computing facilities, as well as advances in computational fluid dynamics, direct numerical simulation of fully nonlinear and three-dimensional dynamo processes has become possible. St. Pierre [9] found the first dynamically self-consistent strong-field dynamo solutions, albeit with a simplified geometry and idealized boundary conditions. Jones *et al.* [10] investigated dynamically self-consistent dynamo solutions in a spherical geometry for a parameter regime similar to that of the Earth, but with only a limited selection of nonaxisymmetric modes (the so-called "2.5-dimensional" dynamo model). Recently, Glatzmaier and Roberts [1–4] found fully three-dimensional dynamo solutions.

Although the Glatzmaier–Roberts model (the GR-model) represents a great advance in numerical modeling of the geodynamo, many fundamental problems remain to be addressed. In this paper we present a numerical model for studying the geodynamo which, while similar to the GR-model in some respects (for example, we retain a complete set of azimuthal modes), includes some significant differences that we conjecture to be important for better approximating the Earth's core within computationally feasible parameter regimes. We have also adopted different numerical algorithms for better computational performance.

Two problems are of particular importance in constructing our numerical model. The first is the force balance in the Earth's fluid core, which is described by the momentum equation,

$$(\partial_t + \mathbf{v}\cdot\nabla)\mathbf{v} + 2\boldsymbol{\Omega}\times\mathbf{v} = -\nabla p + \frac{1}{\rho}\mathbf{J}\times\mathbf{B} + \frac{\Delta\rho}{\rho}\mathbf{g} + \nu\nabla^2\mathbf{v}, \tag{1.2}$$

where p is the modified pressure, $\Delta\rho$ is the density variation, ν is the kinematic viscosity of the fluid, and $\mathbf{g}$ is the gravitational acceleration. In a rapidly rotating system, the fluid inertia and the viscous force are very small compared to the Coriolis force. In the Earth's core, for example, the Ekman number E that describes the ratio of the viscous force to the Coriolis force is very small,

$$E \equiv \frac{\nu}{2\Omega r_o^2} \sim \mathcal{O}(10^{-15}), \tag{1.3}$$

based on the molecular kinematic viscosity of the core fluid (r_o is the mean radius of the core–mantle boundary). Therefore, one expects that the Coriolis force, the Lorentz force, and the buoyancy force $\Delta\rho\mathbf{g}/\rho$ will balance to leading order in a strong-field dynamo.

However, the azimuthal component of the Lorentz force integrated over any cylindrical surface Σ coaxial with the rotation axis across the fluid core (the "Taylor cylinders"; see Fig. 1) can only be balanced by inertia and local viscous stress (provided that the buoyancy force is radial),

$$\int_\Sigma dS(\mathbf{J}\times\mathbf{B})_\phi = \int_\Sigma dS\rho\left[\frac{D\mathbf{v}}{Dt}\right]_\phi - \int_\Sigma dS\rho\nu(\nabla^2\mathbf{v})_\phi, \tag{1.4}$$

where the subscript ϕ denotes the azimuthal components of the forces in the spherical coordinate system (r, θ, ϕ).

The simplest approach is to neglect the viscous force and inertia in the momentum balance (1.2) (the "magnetostrophic balance"). Taylor [11] showed that with this approximation, the velocity field can be uniquely determined if the constraint

$$T_B \equiv \int_\Sigma dS(\mathbf{J}\times\mathbf{B})_\phi = 0 \tag{1.5}$$

is satisfied. It is clear that the Taylor's condition (1.5) is a singular limit of Eq. (1.4). We call the solution that satisfies (1.5) a Taylor state. Note that T_B is proportional to the axial Lorentz torque acting on Σ (see Section 3); accordingly we also call T_B the Lorentz torque and (1.4) the torque balance equation.

Although we believe that the geodynamo is a strong-field dynamo, we do not expect it to be an exact Taylor state: fluid inertia and viscous forces in the Earth's core cause small departures from the Taylor state. It is therefore important to understand the effect of the two forces in the core dynamics.

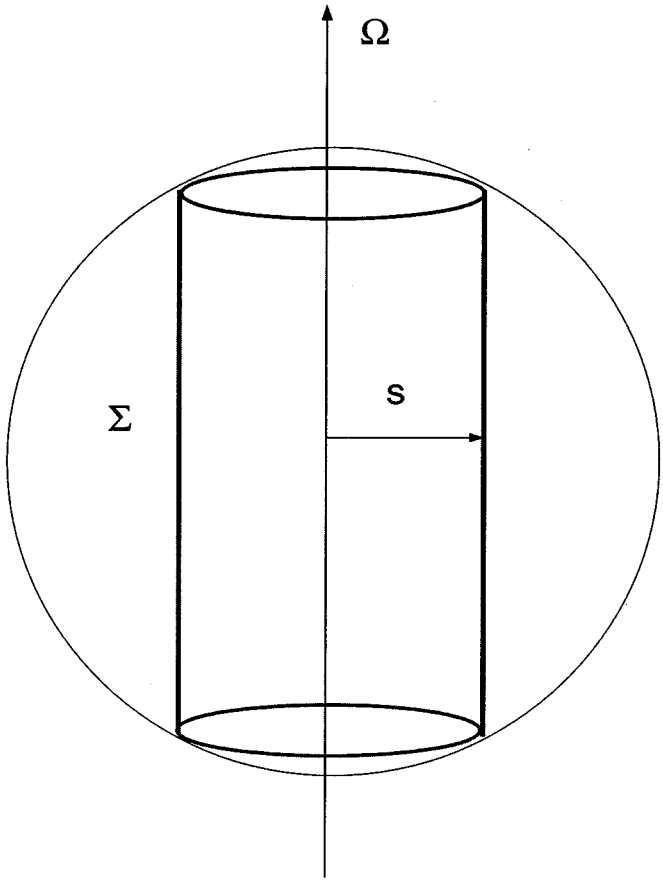

FIG. 1. The cylindrical surface Σ on which the Taylor's constraint is derived.

Unfortunately, it is not computationally feasible to model the geodynamo with the Ekman number in (1.3). Instead, we must seek ways to model the geodynamo with numerically feasible parameters without altering the core dynamics qualitatively. The answer to this problem relies on our finding an appropriate approximation to the force balance in the Earth's core.

This paper is organized as follows. In Section 2, we present the basic system and the corresponding equations. We also discuss in detail the force balance in our system and present the corresponding physical approximations. In Section 3 we describe the numerical method that we use. In Section 4 we discuss tests of simplified versions of the code, examining purely thermal convection and the Kumar–Roberts kinematic dynamo. In Section 5, we report the results of a weak-field dynamo and a strong-field dynamo found from the full system.

2. MATHEMATICAL MODEL

We consider a simple mathematical model: an incompressible, electrically conducting fluid in a spherical shell $r_i < r < r_o$ (where r is the radius) which rotates rapidly about a

vertical axis with an angular velocity

$$\mathbf{\Omega} = \Omega \mathbf{1}_z. \tag{2.1}$$

We refer to $r = r_i$ as the inner core boundary and $r = r_o$ as the outer core boundary (or, in the case of the Earth, the core–mantle boundary).

The momentum balance in the fluid shell is described by (1.2). The variations of the magnetic field $\mathbf{B}$ and the temperature perturbation T are described by the equations

$$\left(\partial_t - \eta \nabla^2\right)\mathbf{B} = \nabla \times (\mathbf{v} \times \mathbf{B}), \tag{2.2}$$

$$\left(\partial_t - \kappa \nabla^2\right)T = -\mathbf{v} \cdot \nabla T + Q, \tag{2.3}$$

where η is the magnetic diffusivity, κ is the thermal diffusivity, and Q describes internal heating (or secular cooling). The incompressibility of the fluid and the nonexistence of magnetic monopoles give

$$\nabla \cdot \mathbf{v} = \nabla \cdot \mathbf{B} = 0. \tag{2.4}$$

We impose a constant incoming heat flux at the inner core boundary r_i by a prescribed temperature gradient

$$h_T \equiv -\left[\frac{\partial T}{\partial r}\right]_{r=r_i}. \tag{2.5}$$

The internal heating Q is assumed to be

$$Q \equiv \frac{\epsilon h_T \kappa}{r_o}, \tag{2.6}$$

where $\epsilon \ll 1$ ($\epsilon = 0.01$ in this study). By (2.5) and (2.6), the system allows the conductive solution

$$T_0(r) = \tilde{T}_0 + r_o h_T \left[\frac{r_{io}^2}{(r/r_o)}\left(1 - \frac{\epsilon}{3} r_{io}\right) - \frac{\epsilon}{6}\left(\frac{r}{r_o}\right)^2\right], \tag{2.7}$$

where

$$r_{io} \equiv \frac{r_i}{r_o} \tag{2.8}$$

is the ratio of the radii of the inner core and the outer core boundaries. The density variation $\Delta\rho$ is given by

$$\frac{\Delta\rho}{\rho} = -\alpha_T (T - T_0) \equiv -\alpha_T \Theta, \tag{2.9}$$

where α_T is the thermal expansion coefficient of the fluid and Θ is the temperature perturbation.

To model the interaction of the Earth's fluid outer core with the solid inner core and the mantle, we permit angular momentum to be exchanged with the mantle above ($r > r_o$) and

the inner core below ($r < r_i$). Denoting the angular momentum of the inner core by $\mathbf{M}_i$ and the angular momentum of the mantle by $\mathbf{M}_m$ in the co-rotating frame, we have (see, e.g., Goldstein [12])

$$\frac{d}{dt}\mathbf{M}_{i,m} + \mathbf{\Omega} \times \mathbf{M}_{i,m} = \mathbf{\Gamma}_B + \mathbf{\Gamma}_v + \mathbf{\Gamma}_p, \tag{2.10}$$

where $\mathbf{\Gamma}_B$, $\mathbf{\Gamma}_v$, and $\mathbf{\Gamma}_p$ are the magnetic, viscous, and pressure torques acting on the boundaries, respectively. The pressure torque $\mathbf{\Gamma}_p$ vanishes on spherical boundaries.

Denoting the deviation of the temperature from the mean state by Θ, using the radius r_o of the outer core boundary as the length scale, the magnetic diffusive time $\tau = r_o^2/\eta$ as the time scale, $\mathcal{B} = (2\Omega\mu\rho\eta)^{1/2}$ as the magnetic field scale, and $h_T r_o$ as the temperature scale, we obtain the nondimensional equations

$$R_o(\partial_t + \mathbf{v}\cdot\nabla)\mathbf{v} + \mathbf{1}_z \times \mathbf{v} = -\nabla p + \mathbf{J}\times\mathbf{B} + E\nabla^2\mathbf{v} + R_{th}\Theta\mathbf{r}, \tag{2.11}$$

$$\left(\partial_t - \nabla^2\right)\mathbf{B} = \nabla\times(\mathbf{v}\times\mathbf{B}), \tag{2.12}$$

$$\left(\partial_t - q_\kappa\nabla^2\right)\Theta = -\mathbf{v}\cdot\nabla[T_0(r) + \Theta], \tag{2.13}$$

where $\mathbf{J}$ and T_0 are the nondimensional forms of (1.1) and (2.7), respectively. The nondimensional parameters in Eqs. (2.11)–(2.13) are the Ekman number E, the magnetic Rossby number R_o, and the Prandtl number q_κ that describe the intrinsic material properties of the system

$$R_0 \equiv \frac{\eta}{2\Omega r_o^2}, \qquad q_\kappa \equiv \frac{\kappa}{\eta}; \tag{2.14}$$

and the Rayleigh number R_{th} that measures the driving buoyancy force

$$R_{th} \equiv \frac{\alpha_T g_o h_T r_o^2}{2\Omega\eta}. \tag{2.15}$$

The magnetic Rossby number R_o and the Ekman number E are very small in a rapidly rotating fluid,

$$R_o,\, E \ll 1. \tag{2.16}$$

In the Earth's outer core, for example,

$$R_o \sim \mathcal{O}(10^{-9}). \tag{2.17}$$

Consequently, there exist rapidly rotating and slowly decaying modes, with differences of several orders of magnitude in their frequencies and the decay rates, as demonstrated in Appendix A (for a more complete analysis, see a more recent paper by Walker *et al*. [13]). Furthermore, very thin boundary layers develop at the boundaries (Ekman layers) and at the Taylor cylinder tangent to the solid inner core at the equator (Stewartson layers). For a detailed discussion of these boundary layers, we refer the reader to Greenspan [14].

Because of these difficulties, several approximations have been adopted in previous studies, which have direct consequences on the torque balances on the Taylor cylinders,

given by

$$T_B = R_o \int_\Sigma dA \left[\frac{D\mathbf{v}}{Dt}\right]_\phi - E \int_\Sigma dA (\nabla^2 \mathbf{v})_\phi, \tag{2.18}$$

which is the nondimensional form of (1.4).

In the simplest approximation, the inertial modes and the torsional oscillations (in Appendix A) vanish from the system. So do the boundary layers arising from the viscous couplings on the inner and outer boundaries. The physical justification for the approximation is that the fast modes associated with the inertial force are irrelevant to the dynamics under consideration and that the viscosity is negligible in the mainstream flow [15], which is where it is believed dynamo action occurs. With this approximation, the Taylor's constraint (1.5) is used to determine the geostrophic part of the flow. This constraint (1.5) has been recently extended to include non-axisymmetric boundaries [16].

However, the dynamical process in the Earth's core does not follow (1.5) exactly. Tough and Roberts [17] first proposed balancing departures from the Taylor state (1.5) by a weak viscous drag at the boundaries for the slow modes (i.e., the modes with negligible inertia). Braginsky [18] further developed this idea, conjecturing a special solution, the so-called Model-*Z* solution, in which the magnetic field lines align almost parallel to the rotation axis of the Earth. We name this approximation the "viscous-type" approximation in the rest of the paper.

There exist two approaches to incorporating viscous effects: indirectly by restoring the viscous torque in the torque balance [15], or directly by retaining the viscous force in the momentum equation (2.11).

The viscous-type approximation may not be appropriate to the Earth's outer core. Observations of variations in the Earth's rotation rate (length-of-day variations) show that on decadal time scales, changes in the rotation rate of the Earth result from the exchange of axial angular momentum between the fluid core and the solid mantle [19, 20]. It is very unlikely that the viscous friction at the core–mantle boundary is important for the angular momentum exchange, since the time scale for viscous dissipation of the required angular momentum is much longer than the observed decadal time scales.

On the other hand, torsional oscillations, which result from the balance of the inertia and the Lorentz torque T_B in (2.18), are excluded both in the magnetostrophic approximation and in the viscous-type approximation, thus rendering them inappropriate for the short-period geomagnetic secular variations.

Based on the above analysis and the fact that the axial angular momentum M_z depends only on axisymmetric part of the flow, we choose to retain the axisymmetric part of the inertial force in the momentum equation (2.11). Denoting the axisymmetric and non-axisymmetric parts of the function f by $\bar{f}$ and f',

$$\bar{f} \equiv \frac{1}{2\pi} \int_0^{2\pi} f \, d\phi, \qquad \text{and} \qquad f' \equiv f - \bar{f}, \tag{2.19}$$

respectively, we approximate the momentum equation (2.11) as

$$R_o(\partial_t \bar{\mathbf{v}} + \overline{\mathbf{v} \cdot \nabla \mathbf{v}}) + \mathbf{1}_z \times \bar{\mathbf{v}} = -\nabla \bar{p} + \overline{\mathbf{J} \times \mathbf{B}} + E \nabla^2 \bar{\mathbf{v}} + R_{th} \bar{\Theta} \mathbf{r}, \tag{2.20}$$

$$\mathbf{1}_z \times \mathbf{v}' = -\nabla p' + (\mathbf{J} \times \mathbf{B})' + E \nabla^2 \mathbf{v}' + R_{th} \Theta' \mathbf{r}. \tag{2.21}$$

The angular momentum balance (2.10) is also approximated as

$$R_o \frac{d}{dt} M_z = \Gamma_z, \tag{2.22}$$

$$\frac{1}{2} M_{x,y} = \pm \Gamma_{y,x}. \tag{2.23}$$

We refer the reader to Appendix D for detailed expression for the torques and the angular momentum **M**.

To further reduce viscous effects in our system, we apply viscous stress-free boundary conditions (2.27), thus eliminating viscous coupling at the boundaries. Accordingly, viscous effects are of $\mathcal{O}(E)$ in our system.

Our approximation is an extension of the force balance for the torsional oscillations proposed by Taylor [11] in his studies of the Taylor's constraint (1.5). Therefore we call our method here the "inertial-type" approximation in the rest of the paper.

Some previous studies have also analyzed the effect of inertia on the Taylor state. Roberts and Stewartson [21] restored inertia to balance a finite Lorentz torque in their weakly nonlinear analysis of magneto-convection; Jault [22] examined the effect of inertia on the Taylor state in the mean-field dynamo studies; and St. Pierre [9] applied inertia in his fully nonlinear studies of the dynamo in a planar layer system. Glatzmaier and Roberts [3] also include inertia in their model, though it is orders of magnitude smaller than the viscous force, so that torsional oscillations will be strongly damped in their model.

We solve Eqs. (2.20), (2.21), (2.12)–(2.13) with the following boundary conditions. The boundary conditions for the temperature Θ take one of two forms. For the fixed heat flux across the boundaries,

$$\frac{\partial \Theta}{\partial r} = 0, \qquad \text{at } r = r_{io}, 1. \tag{2.24}$$

Alternatively, if the temperature is fixed at the boundaries,

$$\Theta = 0, \qquad \text{at } r = r_{io}, 1. \tag{2.25}$$

Likewise, the boundary conditions of the velocity field **v** may have one of the two following forms. For non-slip boundaries,

$$\mathbf{[v]} = 0, \qquad \text{at } r = r_{io}, 1, \tag{2.26}$$

where **[ ]** denote the difference across the boundaries. Alternatively, if the boundaries are impenetrable and viscous stress-free,

$$\mathbf{1}_n \cdot \mathbf{v} = \mathbf{1}_n \times (\boldsymbol{\sigma}_v \cdot \mathbf{1}_n) = 0, \qquad \text{at } r = r_{io}, 1, \tag{2.27}$$

where $\mathbf{1}_n$ is the norm of the boundaries and $\boldsymbol{\sigma}_v$ is the viscous stress tensor. For the detailed expression of $\boldsymbol{\sigma}_v$ in spherical coordinates, see, e.g., Landau and Lifshitz [23].

The boundary conditions for the magnetic field depend on the electrical conductivity of the boundaries. For the perfectly electrically conducting boundaries,

$$\mathbf{1}_n \cdot \mathbf{B} = \mathbf{1}_n \times \mathbf{J} = 0, \qquad \text{at } r = r_{io}, 1; \tag{2.28}$$

for the perfectly electrically insulating boundaries,

$$[\mathbf{B}] = \mathbf{1}_n \cdot \mathbf{J} = 0, \qquad \text{at } r = r_{io}, 1. \tag{2.29}$$

If the boundaries are finitely electrically conducting, we have

$$[\mathbf{B}] = [\mathbf{1}_n \cdot \mathbf{J}] = [\mathbf{1}_n \times \mathbf{E}] = 0, \qquad \text{at } r = r_{io}, 1, \tag{2.30}$$

where $\mathbf{E}$ is the nondimensional electrical field.

3. NUMERICAL METHOD

Because of (2.4), we introduce the poloidal–toroidal decompositions

$$\mathbf{v} = \nabla \times T_v \mathbf{1}_r + \nabla \times \nabla \times P_v \mathbf{1}_r, \tag{3.1}$$

$$\mathbf{B} = \nabla \times T_b \mathbf{1}_r + \nabla \times \nabla \times P_b \mathbf{1}_r, \tag{3.2}$$

where $\mathbf{1}_r$ is the radial unit vector and T and P are the toroidal and poloidal scalars, respectively. For a given radius r, we expand the variables in spherical harmonics,

$$[P_v, T_v, P_b, T_b]^T = \sum_{m=0,M} \sum_{l=m,L} \left[v_l^m, \omega_l^m, b_l^m, j_l^m\right]^T (r, t) Y_l^m(\theta, \phi) + \text{c.c.}, \tag{3.3}$$

where $Y_l^m(\theta, \phi)$ are the orthonormal spherical harmonic functions and c.c. stands for the complex conjugate. A similar expansion is made for the temperature perturbation $r\Theta$. In our model, the azimuthal truncation order M is in general lower than the meridional trunction order L.

Denoting by $\hat{\mathbf{s}}_1$ the vector of variables in spectral space, and substituting (3.1)–(3.3) into (2.12)–(2.13) and (2.20)–(2.21), we obtain the following partial differential equations for the spectral coefficients,

$$A_1 \frac{\partial}{\partial t} \hat{\mathbf{s}}_1 + A_2 \hat{\mathbf{s}}_1 = \hat{\mathbf{N}}_1, \tag{3.4}$$

where A_1 and A_2 are two matrices of linear radial differential operators, and $\hat{\mathbf{N}}_1$ represents the nonlinear interactions. Detailed expressions are given in Appendix B.

The nonlinear term $\hat{\mathbf{N}}_1$ is solved by the collocation point method via spherical transforms. This method has long been applied in geophysical fluid systems (see, e.g., [24]); for a detailed description of the method, we refer the reader to Canuto *et al.* [25].

The spherical transforms account for most of the CPU time. For example, in our simulation on a CRAY J916, more than 80% of the total CPU is attributed to the spherical transforms. A key issue is therefore to optimize these transforms.

One approach is to develop a fast spherical transform algorithm. With a truncation order $0 \le m, l \le L$, a fast transform needs only $\mathcal{O}[L^2 \log L]$ operations, in contrast to $\mathcal{O}(L^3 \log L)$ operation for standard transforms [26]. Unfortunately, fast transforms are not currently practical because of high overhead and the memory requirement for our model.

Another approach is to parallelize evaluation of the spherical transforms. The spherical transforms can be carried out independently at different radii. To exploit this, we

develop a fourth-order compact finite difference algorithm on nonuniform grid points $\{r_i \mid i = 0, 1, \ldots, N\}$ in radius to resolve possible boundary layers in the system optimally.

For illustration, we consider the second-order differential equation

$$\frac{\partial^2}{\partial r^2} y + f(r) y = 0, \tag{3.5}$$

where f is a known function of r. Introducing

$$\tilde{y} = \frac{\partial y}{\partial r}, \tag{3.6}$$

we approximate Eq. (3.5) as

$$\frac{1}{12h}[y_{i+2} + 9y_{i+1} - 9y_i - y_{i-1}] - \frac{1}{2}[(g\tilde{y})_i + (g\tilde{y})_{i+1}] = 0, \tag{3.7}$$

$$\frac{1}{12h}[\tilde{y}_{i+2} + 9\tilde{y}_{i+1} - 9\tilde{y}_i - \tilde{y}_{i-1}] + \frac{1}{2}[(gfy)_i + (gfy)_{i+1}] = 0, \tag{3.8}$$

for $i = 1, 2, \ldots, N-2$. In the above equations, g_i is the transform between the radius r and the uniform grid space x,

$$g_i \equiv (dr/dx)_{x_i},$$

and h is the mesh size of the uniform grid in x. At the boundaries, we have

$$\pm\frac{1}{2h}[y_{i\pm2} - y_i] - \frac{1}{6}[(g\tilde{y})_i + 4(g\tilde{y})_{i\pm1} + (g\tilde{y})_{i\pm2} = 0, \tag{3.9}$$

$$\pm\frac{1}{2h}[\tilde{y}_{i\pm2} - \tilde{y}_i] + \frac{1}{6}[(gfy)_i + 4(gfy)_{i\pm1} + (gfy)_{i\pm2} = 0, \tag{3.10}$$

for $i = 0, N-1$. To better resolve the boundary layers, we choose the collocation points of the Chebyschev polynomials as the radial grid points

$$\begin{cases} r_i = \frac{1}{2}(1 - r_{io}) \cos N x_i + \frac{1}{2}(1 + r_{io}), \\ x_i = (N - i)\pi/N, \end{cases} \qquad \text{for } i = 0, 1, \ldots, N. \tag{3.11}$$

Denoting by $\hat{\mathbf{s}}_2$ and $\hat{\mathbf{N}}_2$ the values of $\hat{\mathbf{s}}_1$ and $\hat{\mathbf{N}}_1$ at the radial grid points, respectively, we reduce the system (3.4) into a set of ODEs,

$$B_1 \frac{d\hat{\mathbf{s}}_2}{dt} + B_2 \hat{\mathbf{s}}_2 = \hat{\mathbf{N}}, \tag{3.12}$$

where B_1 and B_2 are two linear (time independent) matrices. Because of the small inertia in the system, the norm of B_1 is much smaller than that of B_2. To deal with this stiffness, we solve Eqs. (3.12) by the Crank–Nicolson scheme (a second-order A-stable implicit scheme [27]) for the linear terms, and an Adams-family third-order predictor–corrector algorithm

[28] for the nonlinear terms:

$$\left(B_1+\frac{\Delta t}{2}B_2\right)\tilde{\hat{\mathbf{s}}} = \left(B_1-\frac{\Delta t}{2}B_2\right)\hat{\mathbf{s}}_2^{(k)} + \frac{\Delta t}{12}\left[23\,\hat{\mathbf{N}}_2\left(\hat{\mathbf{s}}_2^{(k)}\right) - 16\,\hat{\mathbf{N}}_2\left(\hat{\mathbf{s}}_2^{(k-1)}\right) + 5\,\hat{\mathbf{N}}_2\left(\hat{\mathbf{s}}^{(k-2)}\right)\right], \tag{3.13}$$

$$\left(B_1+\frac{\Delta t}{2}B_2\right)\hat{\mathbf{s}}_2^{(k+1)} = \left(B_1-\frac{\Delta t}{2}B_2\right)\hat{\mathbf{s}}_2^{(k)} + \frac{\Delta t}{12}\left[5\,\hat{\mathbf{N}}_2\left(\tilde{\hat{\mathbf{s}}}\right) + 8\,\hat{\mathbf{N}}_2\left(\hat{\mathbf{s}}_2^{(k)}\right) - \hat{\mathbf{N}}_2\left(\hat{\mathbf{s}}_2^{(k-1)}\right)\right]. \tag{3.14}$$

By this algorithm, we filter out the fast inertial waves that are irrelevant to the physical processes under consideration. Also, we need to evaluate twice the nonlinear terms per time step with the Adams-family algorithm.

The stability condition (CFL condition) of the algorithm is determined by the nonlinear terms $\hat{\mathbf{N}}$ that are solved explicitly (e.g., [28]),

$$\Delta t|\lambda| \le 1.1, \tag{3.15}$$

where the parameter λ is determined by the nonlinear terms $\hat{\mathbf{N}}$; see (C.6) in Appendix C. The CFL condition (3.15) is tested at each time step in our simulation.

The parallelization of the code is tested on CRAY J916 with four processors. Denoting by τ_N the wall clock time of the simulation with N processors, we found that, as shown in Fig. 2,

$$\tau_1 \approx 3.6\tau_4.$$

4. THERMAL INSTABILITY AND KINEMATIC DYNAMO SOLUTIONS

It is difficult to benchmark our model because there are no three-dimensional, fully nonlinear numerical dynamo solutions in similar systems. However, we are able to test our model against well known studies in thermal instabilities and kinematic dynamos. In particular, we are interested in isolating critical Rayleigh numbers for purely thermal convection and the growth rate of magnetic field perturbations in kinematic dynamos. For all simulations in this paper, we choose

$$R_o = E, \qquad q_\kappa = 1, \qquad r_{io} = 12/35. \tag{4.1}$$

4.1. *Thermal Convection in a Rapidly Rotating Fluid*

Our first test is to study thermal convection by eliminating the magnetic field **B** in our system. We wish to identify, at least in the context of purely thermal convection, the asymptotic regime of the small parameters.

In this simplified system, we assume that the heat flux is fixed at the boundaries, and that the boundaries are impenetrable and "stress-free"; see (2.24), (2.27), and (3.3). With these boundary conditions, there is no coupling across the boundaries, and hence the angular momentum of the fluid shell is conserved. For convenience, we assume a zero axial angular

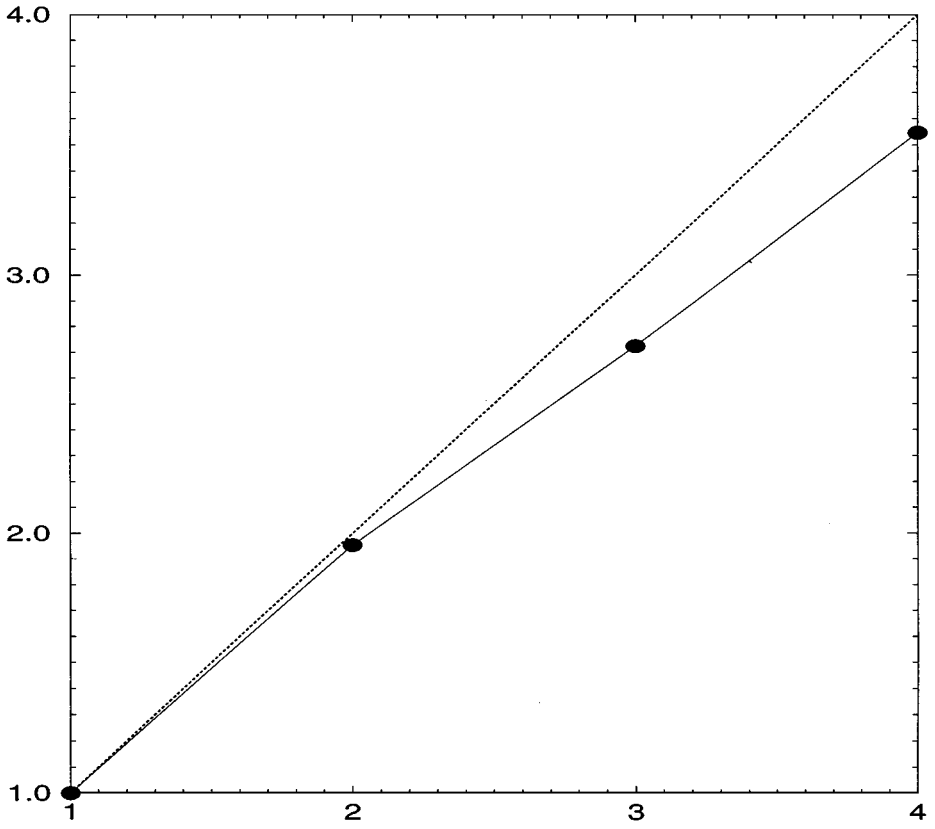

FIG. 2. The test of the parallelization of the code. The horizontal axis is the number N of the processors. The vertical axis is the ratio τ_1/τ_N of the clock time of simulation. The solid circles are the ratios for different numbers of processors used in simulation. The dotted line represents the perfect parallelization (zero overhead).

momentum in the fluid core. Note that the parameters (4.1) imply that

$$p_\kappa \equiv \frac{\nu}{\kappa} = 1. \tag{4.2}$$

The truncation order varies with the Ekman number E, from $L = 28$ for $E = 10^{-3}$ to $L = 42$ for $E = 10^{-5}$. The truncation limit is chosen such that the energy of the cutoff mode is at least four orders of magnitude smaller than the energy peak value.

We start the simulation with small-amplitude random perturbations. We gradually increase R_{th} to a critical value R_{th}^c at which the perturbations stop decaying with time. For comparison with theoretical asymptotic results, we calculate R_{th}^c numerically by the method summarized as follows: for a given Ekman number E, we evaluate the growth rate (or the decay rate) λ of the perturbations for different R_{th}. Then we choose the two Rayleigh numbers R_1 and R_2 with λ_1 and λ_2 closet to zero (i.e., the critical point). The critical Rayleigh number R_{th}^c is then estimated by the extrapolation

$$R_{th}^c = R_1 + \frac{\lambda_1}{\lambda_1 - \lambda_2}(R_2 - R_1).$$

With this method, we obtain

$$R_{th}^c = 115.9, \qquad 248.1, \qquad 450.2 \tag{4.3}$$

for the Ekman numbers

$$E = 10^{-3}, \qquad 10^{-4}, \qquad 10^{-5},$$

respectively. From these values, we derive the asymptotic relation

$$R_{th}^c \approx 10.1 E^{-1/3}. \tag{4.4}$$

This is slightly larger than the early thermal convection result $R^c \sim 8.6956\, E^{-1/3}$ for the Prandtl number (4.2) in a rotating system [6, 29]. However, it is close to a more recent asymptotic result [30]

$$R_{th}^c \sim 10.8 E^{-1/3}.$$

The differences in the results may be partly due to differences in the systems: a rapidly rotating fluid sphere with a uniformly distributed heat source in the fluid has been considered in the previous studies. They may be also caused by the errors in estimating the growth rates λ_1 and λ_2.

When R_{th} is slightly above critical, our solution shows the characteristics of the most unstable mode in linear stability analysis [29]: i.e., the convective flow drifts eastward, and the temperature perturbation is symmetric about the equator.

Our results show that inertia is of secondary importance in the onset of thermal instability and in the slightly super-critical flow. For example, for $E = 10^{-4}$, we do not observe a significant axisymmetric flow in our solutions when R_{th} is slightly super-critical. However, when R_{th} is well above critical (for example, $R_{th} \gtrsim 10 R_{th}^c$), a strong axisymmetric toroidal flow occurs in the system. In Fig. 3 we show a snapshot of the axisymmetric part of the flow. On the right are streamlines of the axisymmetric poloidal flow (the colors represent the sense of circulation) and on the left is the differential rotation

$$\omega_d = v_\phi / r \sin\theta. \tag{4.5}$$

The color scale in the figure shows the (nondimensional) values of ω_d.

4.2. *Kumar–Roberts Kinematic Dynamo Model*

In early studies of dynamo theory, great effort was devoted to understanding the generation of magnetic field with a prescribed flow. In the Kumar–Roberts kinematic dynamo [5], the flow is very simple, yet sufficient to generate magnetic field, provided the magnetic Reynolds number

$$R_m \equiv \frac{\mathcal{V} L}{\eta}, \tag{4.6}$$

where $\mathcal{V}$ is the typical magnitude of the applied flow, is above some critical value. Many subsequent studies in kinematic dynamo theory are extensions of this model [31, 32].

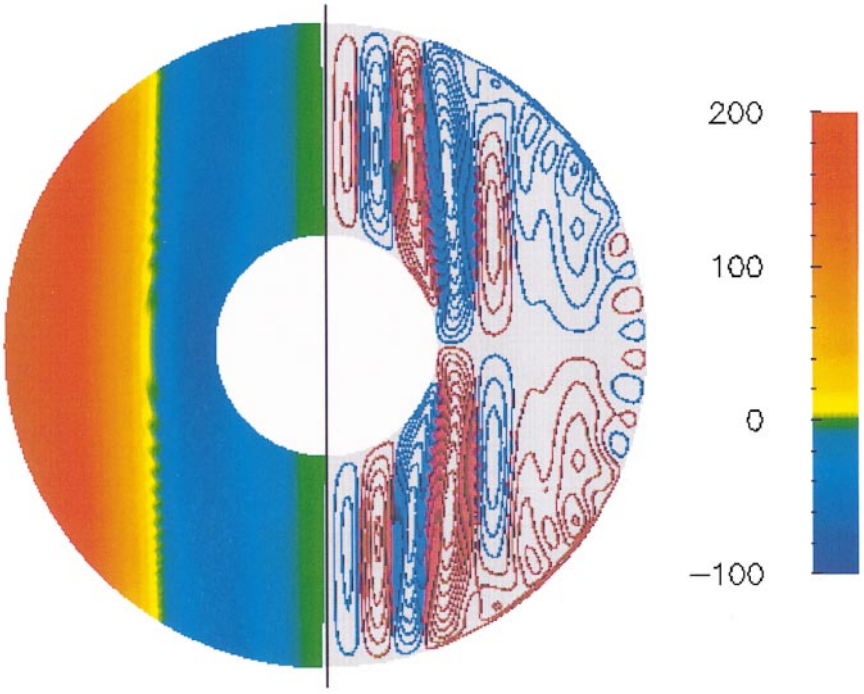

FIG. 3. A snapshot of the differential rotation ω_d (in the left hemispherical shell) and the streamlines of the axisymmetric poloidal flow (in the right hemispherical shell). The color on the left shows the (nondimensional) values of ω_d and the color on the right shows the direction (clockwise/anti-clockwise) of the poloidal flow. The vertical axis is the rotation axis of the system.

We reinvestigate the Kumar–Roberts problem in our spherical shell system with the modified flow

$$\begin{aligned} \omega_1^0 &= -\epsilon_0 \sqrt{4\pi/3}\, x^2(1-x^2), \\ v_2^0 &= \epsilon_1 \sqrt{4\pi/5}\, x^6(1-x^2)^3, \\ v_2^2 &= \sqrt{2\pi/5}\, x^4(1-x^2)^2(\epsilon_2 \cos 3\pi x - i\epsilon_3 \sin 3\pi x), \end{aligned} \tag{4.7}$$

where $\epsilon_{0,1,2,3}$ are constants and

$$x \equiv \frac{r - r_{io}}{1 - r_{io}} \tag{4.8}$$

is the transformed radial coordinate. The coefficients ϵ_i are chosen to be those in the Kumar–Roberts calculations [5]. We also assume that both boundaries are perfect electrical insulators (see (2.29) and (3.3)) and that the magnetic field vanishes at the origin and at infinity.

In kinematic dynamo studies, one needs to solve only the induction equation (2.12), which is linear in **B**. One approach is to solve (2.12) as an eigenvalue problem by assuming

$$\mathbf{B} = \mathbf{B}_0 e^{\sigma t}, \tag{4.9}$$

where σ is the eigenvalue (the complex growth rate) of the mode. Substituting (4.9) into (2.12), one can obtain the eigenvalue equation

$$\det|D_1 - \sigma I| = 0, \tag{4.10}$$

where D_1 is a constant matrix and I is the unitary matrix. Denoting by σ_1 the eigenvalue with the largest real part, we see that dynamo action occurs if

$$\lambda_1 \equiv \Re(\sigma_1) > 0, \tag{4.11}$$

i.e., at least one mode increases exponentially with time. The value λ_1 is referred to as the growth rate of the magnetic field.

Here we integrate the induction equation (2.12) directly from a random initial state, with the truncation order $L = M = 21$ and $N = 36$. After a finite time interval ΔT, the solution is rescaled with the scaling factor f,

$$f = \|\mathbf{B}\|_2 \equiv \left[\int_{V_{\text{core}}} |\mathbf{B}|^2 \, dV\right]^{1/2}, \tag{4.12}$$

where V_{core} is the volume of the spherical shell. After an initial transient period, we can obtain the largest growth rate

$$\lambda_1 = \ln(f)/\Delta T \tag{4.13}$$

and the corresponding most unstable mode. The transient period depends on the values of R_m: our calculations show that this period lasts approximately two magnetic free-decay times, as shown in Fig. 4.

In Fig. 5, we compare our results with those of Holme [32], who solved the eigenvalue problem (4.10) via a second-order finite difference scheme on uniform grid points in radius. Note that our results (the dashed lines) intersect with Holme's (solid lines) approximately at $N = 65$ for all values of R_m, suggesting that the differences are mainly caused by the radial finite difference approximations. In Table I, we list the values of our growth rates, the theoretical results for the free-decay ($R_m = 0$) and the extrapolated results of Holme's eigenvalues. Again, we observe that the results are consistent.

TABLE I
The Growth Rate for the Kumar–Roberts Kinematic Dynamo Model

R_m	0	4000	4500	5500	6000
λ_1	−9.9796	−1.8828	−0.9663	0.9378	1.8712
$\tilde{\lambda}_1$	−10.0257	−2.0096	−1.1331	0.6354	1.5235

Note. λ_1 are the growth rates from our model. $\tilde{\lambda}_1$ are the eigenvalues from the analytical study ($R_m = 0$), and the extrapolated values of the eigenvalues of Holme's kinematic dynamo model (R. Holme, private communication).

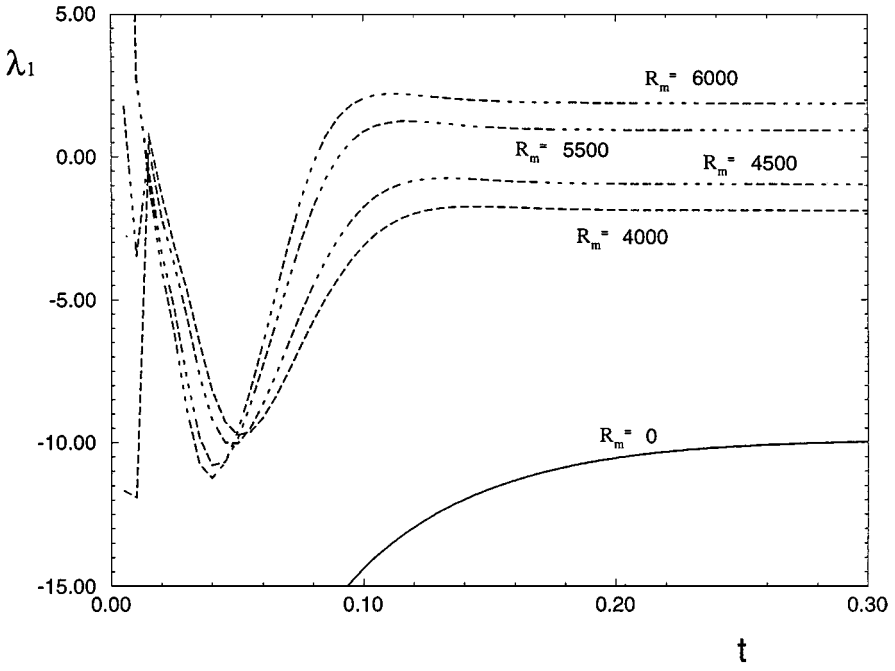

FIG. 4. The growth rate σ of the magnetic field perturbation in the Kumar–Roberts kinematic dynamo for various magnetic Reynolds numbers R_m. The horizontal axis is the (nondimensional) time. Because the free-decay rate ($R_m = 0$) is approximately 10 (see Table I), the nondimensional magnetic free decay time is $t_d \approx 0.1$.

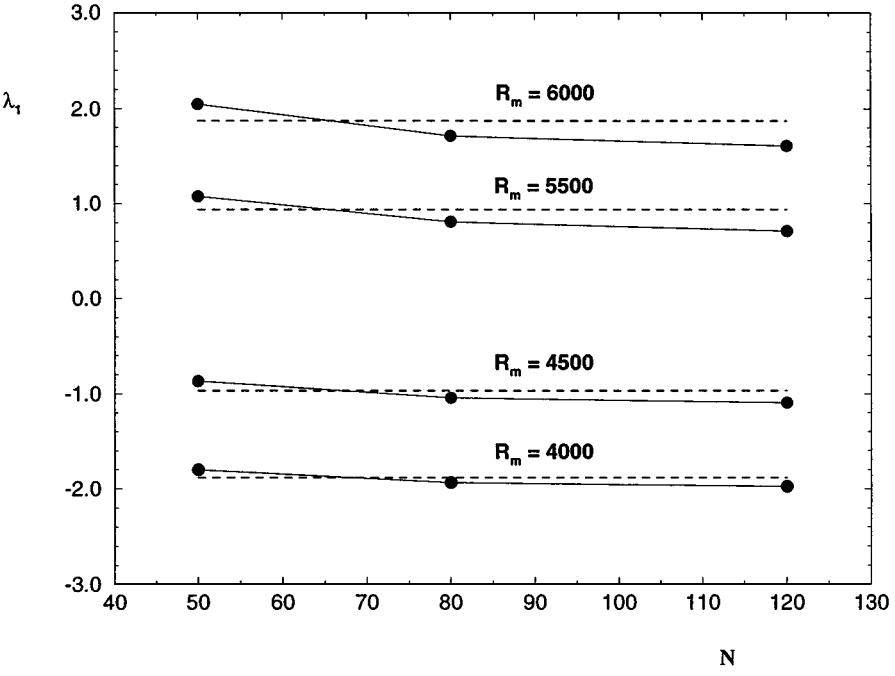

FIG. 5. The comparison of the growth rate λ_1 for the Kumar–Roberts kinematic dynamo model. The dashed lines are the results from our model. The circles are the results from the Holme's eigenvalue model for $N = 50$, 80, 120, where N is the number of grid points in radius in his model (R. Holme, private communication).

5. THERMALLY DRIVEN SELF-CONSISTENT DYNAMOS

In our search for fully dynamically, self-consistent dynamo solutions, we also use fixed heat flux boundary conditions and viscous stress-free boundary conditions. The boundary conditions for the magnetic field vary in our simulation; we address this later in this section.

The magnetic Rossby number R_o and the Ekman number E vary in our simulation. We start with the value

$$E = 10^{-4}. \tag{5.1}$$

The corresponding critical Rayleigh number for the thermal convection is given in (4.3).

As shown for the Kumar–Roberts model in Section 4, dynamo action occurs if the driving flow is sufficiently strong, or equivalently, if the (thermally driven) convection is sufficiently vigorous, thus suggesting that dynamo action occurs if the Rayleigh number R_{th} reaches a certain threshold value $R_{th}^m > R_{th}^c$, and that the magnitude of the generated magnetic field increases with R_{th}.

However, when the Lorentz force is comparable to the Coriolis force, the critical value for convection decreases, as summarized in [6]. Thus one may expect that if the generated magnetic field is sufficiently strong, dynamo action may persist at subcritical Rayleigh numbers, i.e., at $R_{th} < R_{th}^c$. This was shown analytically by Childress and Soward [33] in a rapidly rotating planar layer system, and demonstrated numerically by St. Pierre [9].

Guided by these studies, we start our dynamo simulation with small-amplitude random perturbations to seek weak-field dynamos, and with large-amplitude random states to seek strong-field dynamos.

5.1. *Weak-Field Dynamo Solutions*

For the weak-field dynamo study, we assume that the inner core is a perfect electrical conductor, and that the mantle is a perfect electrical insulator; see (2.28) and (2.29). Since the magnetic stress vanishes at both boundaries, the total angular momentum of the fluid is conserved, a condition that is well satisfied in our calculations.

We integrate the solution from a small-amplitude, random initial state with supercritical R_{th}. Initially, the magnetic field decays exponentially, while the velocity and temperature perturbations develop to a finite amplitude state, indicating a non-magnetic thermal convective solution. The decay rate of the magnetic field perturbations decreases as R_{th} increases. The magnetic field stops decaying when R_{th} reaches a value R_{th}^m:

$$R_{th}^m \approx 14 R_{th}^c. \tag{5.2}$$

In Fig. 6, we show the variation of the L_2-norm $\mathcal{B}$ of the magnetic field for $R_{th} = 14 R_{th}^c$ (the solid line), and for $R_{th} = 13 R_{th}^c$ (the dashed line). Note that dynamo action occurs first at R_{th}^m.

The magnetic field is weak, in the sense that the local Elsasser number $\tilde{\Lambda}$ is very small in the fluid core:

$$\tilde{\Lambda} \equiv \left| \frac{\mathbf{J} \times \mathbf{B}}{\mathbf{1}_z \times \mathbf{V}} \right| \leq 2 \times 10^{-3}. \tag{5.3}$$

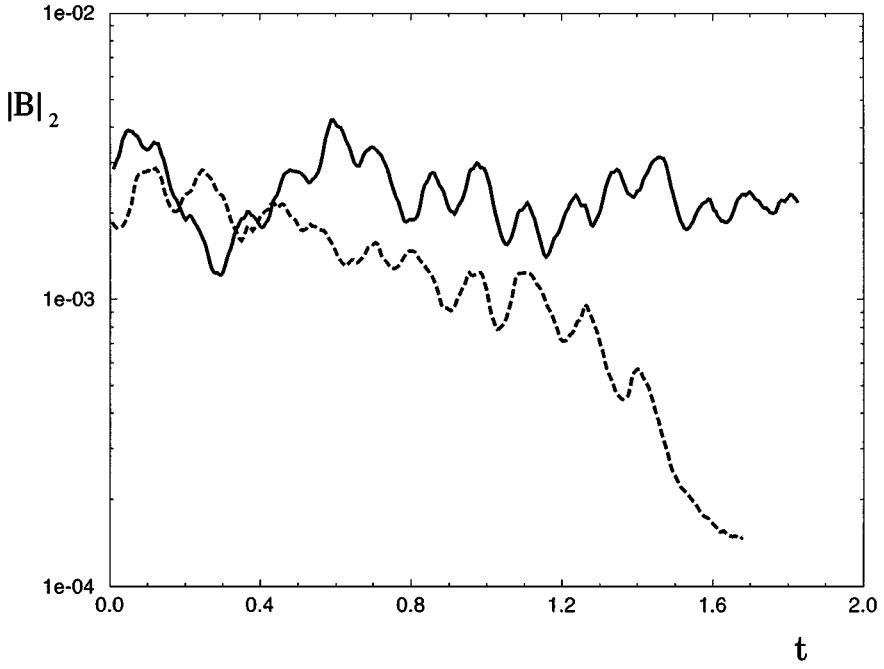

FIG. 6. The L_2-norm of magnetic field **B** perturbations at different values of the Rayleigh number R_{th}. The solid line is for $R_{th} = 14R^c_{th}$, while the dashed line is for $R_{th} = 13R^c_{th}$. The time t is scaled with the magnetic free-decay time t_d.

Also, the total magnetic energy E_B is small compared with the total kinetic energy E_V:

$$\frac{E_B}{E_V} \approx 0.1. \tag{5.4}$$

The length scale of the magnetic field is very small, as shown by a snapshot of the radial magnetic field at the outer core boundary (Fig. 7).

The field is generated near the inner core boundary and spreads spirally toward the outer core boundary. The zonal propagation of the magnetic field varies radially: the field drifts eastward (in the direction of the rotation of the system) near the outer core boundary, and drifts westward near the inner core boundary.

Compared with the imposed flow (4.7) in the Kumar–Roberts dynamo model, the convective flow in our system is far more efficient in the magnetic field generation: the local magnetic Reynolds number

$$\tilde{R}_m \equiv \frac{1}{2\pi} \int_0^{2\pi} d\phi \frac{|\nabla \times (\mathbf{v} \times \mathbf{B})|}{|\nabla^2 \mathbf{B}|} \leq 20 \tag{5.5}$$

is only slightly above the lower limit required for the onset of dynamo action [34], but much smaller than those values in the Kumar–Roberts dynamo solutions (see Table I).

This indicates that the weak magnetic field interacts dynamically with the flow. To illustrate this, we show, in Fig. 8, a snapshot of the axisymmetric flow of the solution. Compared with that of the purely thermal convection (Fig. 3), we observe significant differences in the differential rotation ω_d. This is partly caused by a small magnetic torque T_B on the Taylor cylinders that can only be balanced by a small axial inertial force ($\sim R_o$).

Although our system differs from the systems studied previously, such as rotating annulus [35] and rotating spheres [36], our solutions share some properties with the weak-field dynamo solutions in those systems. For example, the toroidal field is comparable to the poloidal field, and the differential rotation decreases with the depth.

5.2. *Strong-Field Dynamo Solutions*

We study strong-field dynamos at higher Rayleigh numbers. To approximate more closely the Earth's outer core, we assume that the electrical conductivity of the inner core is the same as that of the fluid core ($\eta_i = \eta$). Hollerbach and Jones [37] demonstrated that a finitely conducting solid inner core is important in their dynamo solutions.

We assume also that there is a conductive layer above the outer core boundary with (nondimensional) thickness

$$\delta_m = 2/35$$

and magnetic diffusivity

$$\eta_m = 400\eta.$$

The finite Lorentz stress on the boundaries generates couplings across the boundaries.

To avoid high truncation for the initial transient period and to reduce the CPU time for the process, we introduce a hyper-dissipation,

$$\nu = \begin{cases} \nu_0, & \text{for } l \le l_0, \\ \nu_0\left[1 + \epsilon(l - l_0)^2\right], & \text{for } l > l_0; \end{cases} \tag{5.6}$$

similarly for magnetic diffusion η and thermal conductivity κ. As the simulation proceeds, we gradually reduce the hyper-dissipation by either increasing l_0 or decreasing ϵ. Our application of the hyper-dissipation follows from Glatzmaier and Roberts [1], though the form (5.6) is weaker than that of Glatzmaier and Roberts.

For mathematical convenience, we apply asymptotic boundary conditions near the origin of the system [5],

$$\left[b_l^m(r),\, j_l^m(r)\right] \sim r^{l+1} \qquad \text{at } r = 0.1 r_{io}. \tag{5.7}$$

The magnetic field boundary conditions at the boundaries are, by (2.30) and (3.3),

$$\begin{aligned} \left[b_l^m\right] = \left[j_l^m\right] = \left[\partial b_l^m / \partial r\right] = 0, \\ \left[\alpha_\eta \left(\partial j_l^m / \partial r\right)\right] = \frac{r}{l(l+1)} H(r)_l^m, \end{aligned} \qquad \text{at } r = 1, r_{io}, \tag{5.8}$$

where

$$\alpha_\eta \equiv \frac{\eta_{i,m}}{\eta} \tag{5.9}$$

denotes the ratio of the magnetic diffusivities across the boundaries and

$$H = \frac{1}{\sin\theta}\frac{\partial}{\partial\phi} B_r[v_\theta] - \frac{1}{\sin\theta}\frac{\partial}{\partial\theta}\sin\theta\, B_r[v_\phi]. \tag{5.10}$$

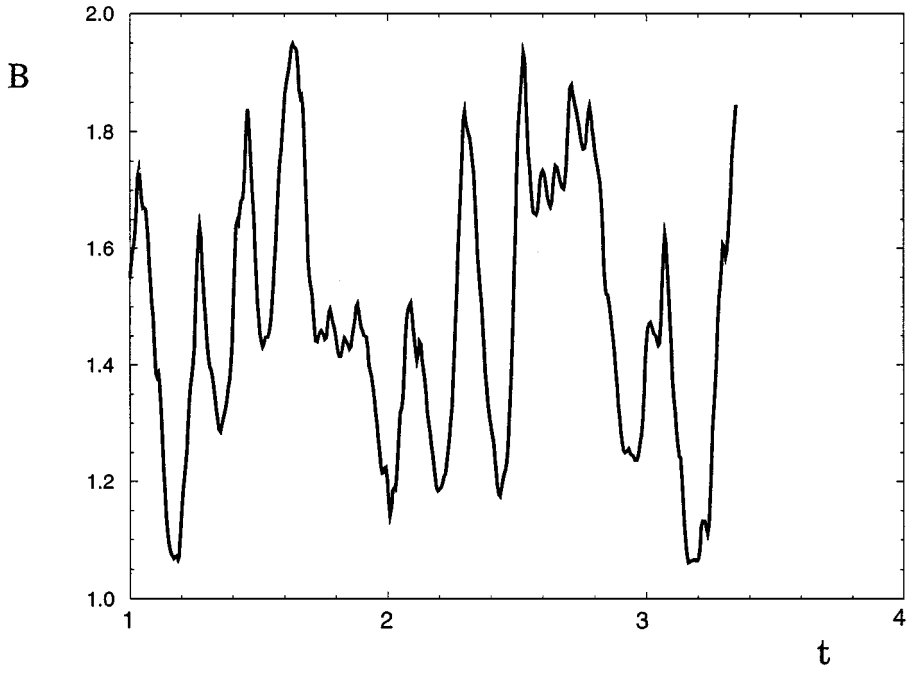

FIG. 9. The L_2-norm of the strong magnetic field solution for $R_o = E = 10^{-4}$. The horizontal coordinate is the time scaled by the magnetic free-decay time τ_d, and the vertical coordinate is the L_2-norm of the magnetic field.

We study strong-field dynamo action for two sets of parameters,

$$E = 10^{-4} \qquad \text{and} \qquad E = 2 \times 10^{-5}. \tag{5.11}$$

In the first case, a strong-field dynamo solution is found when

$$R_{th} \approx 40 R_{th}^c \qquad \text{for } \epsilon = 0.032, l_0 = 5, \tag{5.12}$$

as shown in Fig. 9. In the second case, a strong-field dynamo solution is found when

$$R_{th} \approx 35 R_{th}^c \qquad \text{for } \epsilon = 0.05, l_0 = 5, \tag{5.13}$$

as shown in Fig. 10. In both cases, we choose $L = 40$, $M = 32$, and $N = 40$.

The generated magnetic field is strong: the Lorentz force is comparable to the Coriolis force

$$\tilde{\Lambda} \approx 1 \tag{5.14}$$

in the bulk of the fluid core. The magnetic energy is also much larger than the kinetic energy, with a typical ratio

$$\frac{E_B}{E_v} \approx 2000 \tag{5.15}$$

in the solutions.

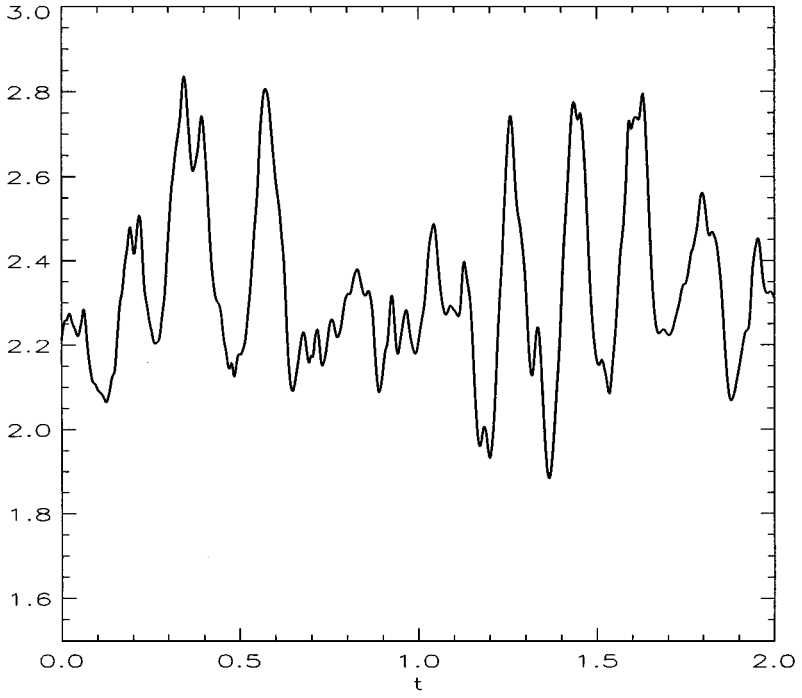

FIG. 10. Similar to the previous figure, but for $R_o = E = 2 \times 10^{-5}$.

In Fig. 11, we show a snapshot of the radial component B_r of the second solution at the outer core boundary. It is dominantly dipolar, with the magnetic field lines entering the fluid core in the northern hemisphere and leaving the fluid core in the southern hemisphere. The field drifts westward at the boundary. These features are very similar to those of the geomagnetic field at the core–mantle boundary inverted from the observations at the surface of the Earth [38].

The configuration of the magnetic field inside the fluid core is simple. In Fig. 12 we show a snapshot of the axisymmetric toroidal magnetic field (in the left hemispherical shell) and the field lines of the axisymmetric poloidal field (in the right hemispherical shell). The poloidal field is predominantly dipolar, while the toroidal field is predominantly quadrupolar. In particular, we observe that the field is very strong in the bulk of the fluid core outside the tangent cylinder.

Our solution differs from that of the Glatzmaier and Roberts [4] inside the fluid core. In their model, the field is strong near the inner core boundary and within the tangent cylinder. Also, the field in their solution displays a more complicated morphology, in particular near the inner core boundary. We discuss these differences elsewhere [39].

6. CONCLUSIONS

In this paper we have presented a numerical model to simulate convective flow in a rapidly rotating spherical shell. We assume that the (axisymmetric) inertia is important in the torque balance (1.4) on the Taylor cylinders, and we minimize the viscous torque on the cylinders by imposing the viscous stress-free boundary conditions.

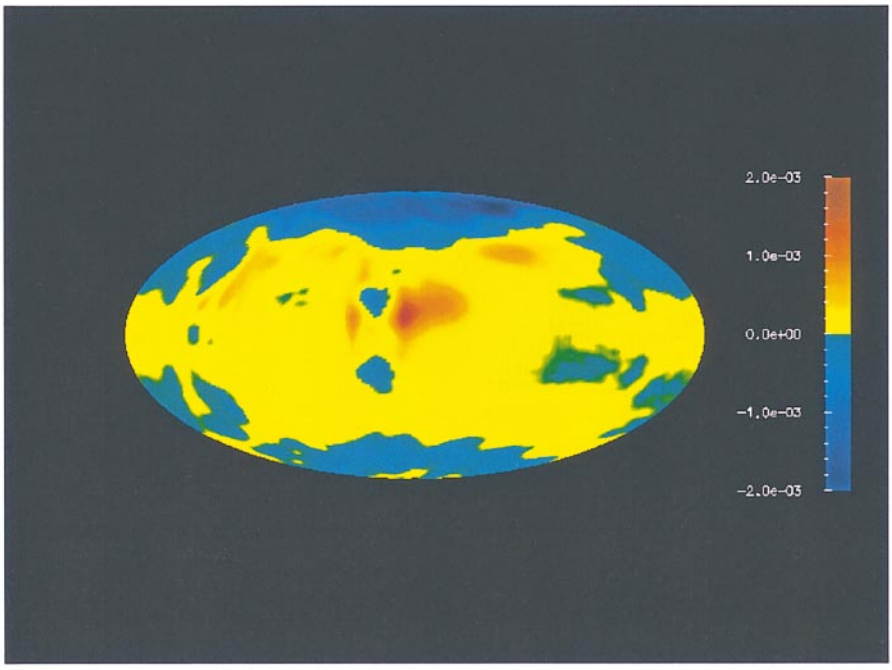

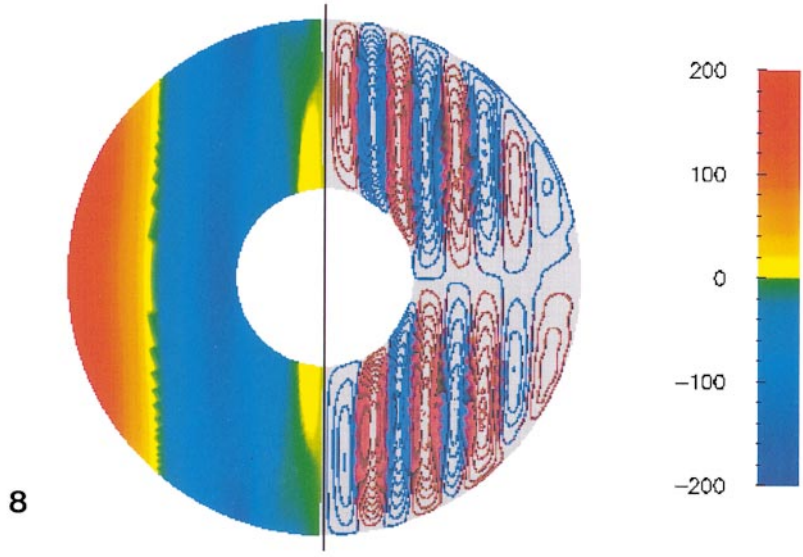

FIG. 7. A snapshot of the radial magnetic field B_r of the weak-field dynamo solution at the outer core boundary $r = 1$.

FIG. 8. A snapshot of the differential rotation ω_d (in the left hemispherical shell) and the streamlines of the axisymmetric poloidal flow (in the right hemispherical shell) of the weak-field dynamo solution.

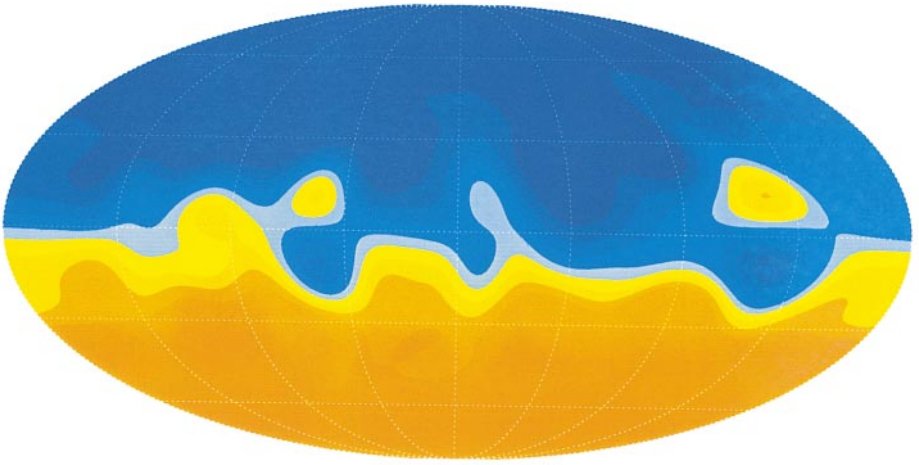

FIG. 11. A snapshot of the radial magnetic field B_r of the strong-field dynamo solution at the core–mantle boundary $r = 1$.

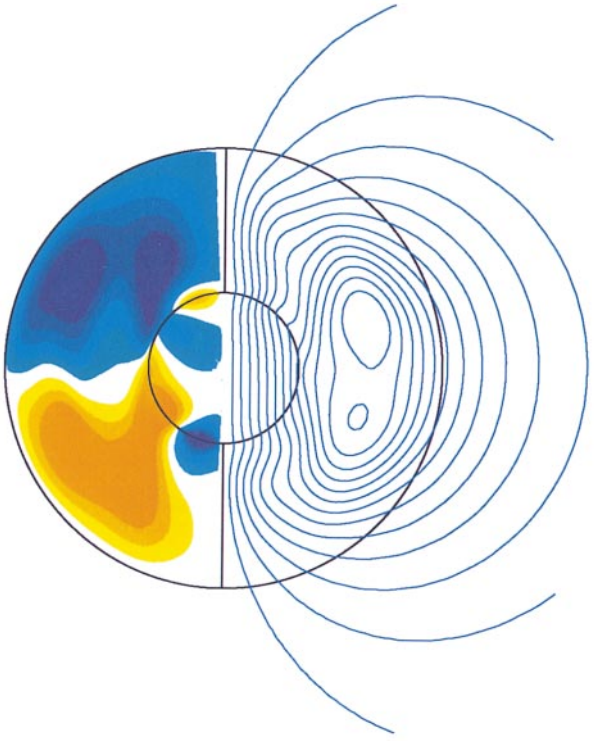

FIG. 12. A snapshot of the axisymmetric part of magnetic field in the strong-field dynamo solution for $R_o = E = 2 \times 10^{-5}$. The toroidal field is shown in the left hemispherical shell and the magnetic field lines of the poloidal field are shown in the right hemispherical shell. The colors on the left represent the strength of the toroidal field.

We use a mixed spectral–finite difference scheme in space and a multi-step predictor–corrector algorithm in time. The time step is controlled by Alfvén modes that result from a balance of the inertial force and the Lorentz force (CFL condition). We have tested our model against purely thermal convection and the Kumar–Roberts kinematic dynamo, and have found good agreement.

We have studied weak-field dynamos in a simple, mechanically isolated system by allowing an electrically perfectly conducting inner core and an electrically perfectly insulating mantle. We found a weak-field dynamo solution at the supercritical Rayleigh number $R_{th}^m = 14R_{th}^c$ for $R_o = E = 10^{-4}$. The Lorentz force is negligible compared with the Coriolis force, and the magnetic energy is small compared with the kinetic energy. The magnetic field is dominantly equatorial dipolar ($l = m = 1$ mode in spherical harmonic expansion) at the outer core boundary. The length scale of the field is very small in the fluid core.

We have studied strong-field dynamos in a system closer to the Earth: we include a finitely conducting solid inner core and a finitely conducting layer at the top of the fluid core. The exchange of the angular momentum across the boundaries is carried out by the magnetic torque acting on the boundaries. In this system, we found two strong-field dynamo solutions: one for $R_{th} \approx 40R_{th}^c$, $R_o = E = 10^{-4}$ and one for $R \approx 35R_{th}^c$, $R_0 = E = 2 \times 10^{-5}$. The generated magnetic field is strong: the Lorentz force is comparable to the Coriolis force in the bulk of the fluid core and the magnetic energy is three orders of magnitude larger than the kinetic energy.

At the outer core boundary, our strong-field dynamo solution for $R_o = E = 2 \times 10^{-5}$ is similar to the observed geomagnetic field in many aspects: the field is dominantly dipolar and drifts westward. Inside the fluid core, our solution differs greatly from the solutions of Glatzmaier and Roberts [39]. In our solution, the field is dominantly generated in the bulk of the fluid core outside the tangent cylinder, while the field in the Glatzmaier–Roberts dynamo solution is generated near the inner core boundary and inside the tangent cylinder.

We have demonstrated [39] that, when a strong viscous coupling is introduced on the boundaries while the inertia is kept unchanged, the dynamo solutions undergo a transition from our solution to the solutions qualitatively the same as the Glatzmaier–Roberts dynamo solutions.

Although these studies (in which the fluid inertia is much larger than that appropriate for the Earth's core) help us to understand the effect of strong viscous couplings on dynamo processes in the fluid core, we still need to investigate the effect of inertia on the dynamo solutions. One of our goals is to study the effect of the inertia on the fast varying (i.e., short time scale) flows so that we can apply our results to the geomagnetic secular variations by appropriate asymptotic extrapolations.

APPENDIX A: NORMAL MODE ANALYSIS

We consider a simple system: an infinite layer of electrically conducting fluid rotating about vertical, with a prevailing uniform magnetic field $\mathbf{B}_0$. Introducing small normal mode perturbations,

$$f(\mathbf{r}, t) = f_0 e^{i\mathbf{k}\cdot\mathbf{r}+\lambda t},$$

and neglecting the nonlinear terms of the perturbations, we may obtain from (2.11)–(2.12)

the dispersion relation

$$(\lambda + k^2)\left(R_o\lambda + k^2 E \pm i k_z/k\right) + \Lambda(\mathbf{k}\cdot\mathbf{B}_0)^2 = 0. \tag{A.1}$$

There are two limiting cases that are particularly interesting. If the wave number $\mathbf{k}$ is almost perpendicular to $\mathbf{B}_0$, i.e., the perturbation is decoupled from the prevailing magnetic field, we may obtain from (A.1) the "kinematic" modes

$$\lambda = \frac{1}{R_o}\left(-k^2 E \pm i k_z/k\right), \tag{A.2}$$

together with the (magnetic) free decay modes

$$\lambda = -k^2. \tag{A.3}$$

The modes (A.2) are called inertial modes and result from a balance between the Coriolis force and the inertial force. The decay rate and the oscillation frequency of the inertial modes differ by a factor of E^{-1}.

If the perturbations are almost invariant in the direction of the rotation axis, i.e., $k_z \approx 0$, we have the magnetic modes

$$\lambda = -\frac{k^2}{2} \pm i|\mathbf{k}\cdot\mathbf{B}_0|\left[\frac{1}{R_o} - \frac{k^4}{4(\mathbf{k}\cdot\mathbf{B}_0)^2}\right]^{1/2}, \tag{A.4}$$

which are often called torsional oscillations in geomagnetism [40]. They result from a balance between the inertial force and the Lorentz force. The decay rate and the oscillation frequency of the magnetic modes differ by a factor of $R_o^{-1/2}$.

APPENDIX B: SPHERICAL HARMONIC EXPANSIONS

B.1. *Components of the Fluid Flow and the Magnetic Field*

Using (3.1), we obtain the following expressions for the components of the flow $\mathbf{v}$ and the vorticity $\boldsymbol{\omega} = \nabla \times \mathbf{v}$,

$$r^2 v_r = -\hat{L} P_v, \tag{B.1}$$

$$r\sin\theta\, v_\theta = \sin\theta \frac{\partial}{\partial\theta}\frac{\partial P_v}{\partial r} + \frac{\partial T_v}{\partial\phi}, \tag{B.2}$$

$$r\sin\theta\, v_\phi = \frac{\partial}{\partial\phi}\frac{\partial P_v}{\partial r} - \sin\theta\frac{\partial T_v}{\partial\theta}, \tag{B.3}$$

$$r^2 \omega_r = -\hat{L} T_v, \tag{B.4}$$

$$r\sin\theta\, \omega_\theta = \sin\theta\frac{\partial}{\partial\theta}\frac{\partial T_v}{\partial r} - \frac{\partial}{\partial\phi}\left(\frac{\partial^2}{\partial r^2} + \frac{\hat{L}}{r^2}\right)P_v, \tag{B.5}$$

$$r\sin\theta\, \omega_\phi = \frac{\partial}{\partial\phi}\frac{\partial T_v}{\partial r} + \sin\theta\frac{\partial}{\partial\theta}\left(\frac{\partial^2}{\partial r^2} + \frac{\hat{L}}{r^2}\right)P_v, \tag{B.6}$$

where

$$\hat{L} \equiv \frac{1}{\sin\theta}\frac{\partial}{\partial\theta}\sin\theta\frac{\partial}{\partial\theta} + \frac{1}{\sin^2\theta}\frac{\partial^2}{\partial\phi^2} \tag{B.7}$$

is the angular momentum operator. Replacing (P_v, T_v) by (P_b, T_b) in the above equations, we obtain similar expressions for the components of the magnetic field **B** and the current density **J**.

B.2. *The Equations of the Magnetic Field B and the Temperature* Θ

Substituting the expansion (3.3) into (B. 1)–(B. 6), and then into $\mathbf{1}_r\cdot$ (2.12), $\mathbf{1}_r\cdot\nabla\times$ (2.12), and (2.13), we obtain the following equations for the spectral coefficients of the fields,

$$\left\{\frac{\partial}{\partial t} - \left[\frac{\partial^2}{\partial r^2} - \frac{l(l+1)}{r^2}\right]\right\} b_l^m = \frac{r^2}{l(l+1)} f_3^{lm}, \tag{B.8}$$

$$\left\{\frac{\partial}{\partial t} - \left[\frac{\partial^2}{\partial r^2} - \frac{l(l+1)}{r^2}\right]\right\} j_l^m = \frac{r^2}{l(l+1)} f_4^{lm}, \tag{B.9}$$

$$\left\{\frac{\partial}{\partial t} - q_\kappa\left[\frac{\partial^2}{\partial r^2} - \frac{l(l+1)}{r^2}\right]\right\} T_l^m = r f_5^{lm}, \tag{B.10}$$

where

$$f_3 = \mathbf{1}_r\cdot[\nabla\times(\mathbf{v}\times\mathbf{B})], \tag{B.11}$$

$$f_4 = \mathbf{1}_r\cdot[\nabla\times\nabla\times(\mathbf{v}\times\mathbf{B})], \tag{B.12}$$

$$f_5 = -\mathbf{v}\cdot\nabla T_0 - \mathbf{v}\cdot\nabla\Theta. \tag{B.13}$$

B.3. *The Momentum Equations*

Because the Coriolis term in (2.11) causes the coupling between adjacent spectral coefficients (v_l^m, ω_l^m), we divide the coefficients into two groups according to their symmetry properties,

$$\left[v_{l_1}^{m(s)}, v_{l_1}^{m(a)}\right]^T = \left[v_{m+2l_1}^m, v_{m+2l_1+1}^m\right]^T, \tag{B.14}$$

and similarly for ω_l^m.

Taking $\mathbf{1}_r\cdot\nabla\times$ (2.11) and $\mathbf{1}_r\cdot\nabla\times\nabla\times$ (2.11), applying the spherical harmonic transform (3.3) and the symmetry parity (B.14), and the recurrence relations

$$\cos\theta Y_l^m(\theta,\phi) = c_{l+1}^m Y_{l+1}^m(\theta,\phi) + c_l^m Y_{l-1}^m(\theta,\phi), \tag{B.15}$$

$$\sin\theta\frac{\partial}{\partial\theta}Y_l^m(\theta,\phi) = l c_{l+1}^m Y_{l+1}^m(\theta,\phi) - (l+1)c_l^m Y_{l-1}^m(\theta,\phi), \tag{B.16}$$

$$c_l^m = \sqrt{\frac{(l-m)(l+m)}{(2l-1)(2l+1)}}, \tag{B.17}$$

we obtain the following compact momentum equations for the spectral coefficients of the toroidal and the poloidal flow,

$$\left\{R_o\frac{\partial}{\partial t}-E\left[\frac{\partial^2}{\partial r^2}-\frac{l(l+1)}{r^2}\right]-\frac{im}{l(l+1)}\right\}\omega_{l_1}^{m(a)}-\frac{(l-1)}{l}c_l^m\left(\frac{\partial}{\partial r}-\frac{l}{r}\right)v_{l_1}^{m(s)}$$
$$-\frac{(l+2)}{(l+1)}c_{l+1}^m\left(\frac{\partial}{\partial r}+\frac{l+1}{r}\right)v_{l_1+1}^{m(s)}=\frac{r^2}{l(l+1)}f_1^{lm}, \tag{B.18}$$

$$-\left\{R_o\frac{\partial}{\partial t}-E\left[\frac{\partial^2}{\partial r^2}-\frac{l(l+1)}{r^2}\right]-\frac{im}{l(l+1)}\right\}\left[\frac{\partial^2}{\partial r^2}-\frac{l(l+1)}{r^2}\right]v_{l_1}^{m(s)}$$
$$-\frac{(l-1)}{l}c_l^m\left(\frac{\partial}{\partial r}-\frac{l}{r}\right)\omega_{l_1-1}^{m(a)}-\frac{(l+2)}{(l+1)}c_{l+1}^m\left(\frac{\partial}{\partial r}+\frac{l+1}{r}\right)\omega_{l_1}^{m(a)}$$
$$=\frac{r^2}{l(l+1)}f_2^{lm}+\left[R_{th}T_l^m+R_{co}C_l^m\right], \tag{B.19}$$

and

$$\left\{R_o\frac{\partial}{\partial t}-E\left[\frac{\partial^2}{\partial r^2}-\frac{l(l+1)}{r^2}\right]-\frac{im}{l(l+1)}\right\}\omega_{l_1}^{m(s)}-\frac{(l-1)}{l}c_l^m\left(\frac{\partial}{\partial r}-\frac{l}{r}\right)v_{l_1-1}^{m(a)}$$
$$-\frac{(l+2)}{(l+1)}c_{l+1}^m\left(\frac{\partial}{\partial r}+\frac{l+1}{r}\right)v_{l_1}^{m(a)}=\frac{r^2}{l(l+1)}f_1^{lm}, \tag{B.20}$$

$$-\left\{R_o\frac{\partial}{\partial t}-E\left[\frac{\partial^2}{\partial r^2}-\frac{l(l+1)}{r^2}\right]-\frac{im}{l(l+1)}\right\}\left[\frac{\partial^2}{\partial r^2}-\frac{l(l+1)}{r^2}\right]v_{l_1}^{m(a)}$$
$$-\frac{(l-1)}{l}c_l^m\left(\frac{\partial}{\partial r}-\frac{l}{r}\right)\omega_{l_1}^{m(s)}-\frac{(l+2)}{(l+1)}c_{l+1}^m\left(\frac{\partial}{\partial r}+\frac{l+1}{r}\right)\omega_{l_1+1}^{m(s)}$$
$$=\frac{r^2}{l(l+1)}f_2^{lm}+\left[R_{th}T_l^m+R_{co}C_l^m\right], \tag{B.21}$$

where

$$f_1=\mathbf{1}_r\cdot\nabla\times[\mathbf{J}\times\mathbf{B}-R_o\boldsymbol{\omega}\times\mathbf{v}], \tag{B.22}$$

$$f_2=\mathbf{1}_r\cdot\nabla\times\nabla\times[\mathbf{J}\times\mathbf{B}-R_o\boldsymbol{\omega}\times\mathbf{v}]. \tag{B.23}$$

Note that (f_1, f_2) in (B.22)–(B.23) are similar to (f_3, f_4) in (B.11)–(B.12). Equations (B.8)–(B.10) and (B.18)–(B.21) can be written in a generalized form (3.4).

APPENDIX C: NONLINEAR EIGENVALUES OF THE NONLINEAR TERMS

Denote by $\mathbf{f}$ the flow of the system

$$\mathbf{f}=(\mathbf{v},\mathbf{B},\Theta)^T. \tag{C.1}$$

Assuming that

$$\mathbf{f}'=(\mathbf{v}',\mathbf{B}',\Theta')^T \tag{C.2}$$

is a small departure from the state (C.1), retaining and linearizing the terms in (2.11)–(2.13) that are solved explicitly, and replacing ∂_t with the eigenvalue λ, we obtain

$$(\lambda + \mathbf{v}\cdot\nabla)\mathbf{v}' = -\mathbf{v}'\cdot\nabla\mathbf{v} + \frac{1}{R_o}(\mathbf{B}\cdot\nabla\mathbf{B}' + \mathbf{B}'\cdot\nabla\mathbf{B}) + \mathbf{r}\frac{R_{th}}{R_o}\Theta', \tag{C.3}$$

$$(\lambda + \mathbf{v}\cdot\nabla)\mathbf{B}' = -\mathbf{v}'\cdot\nabla\mathbf{B} + \mathbf{B}\cdot\nabla\mathbf{v}' + \mathbf{B}'\cdot\nabla\mathbf{v}, \tag{C.4}$$

$$(\lambda + \mathbf{v}\cdot\nabla)\Theta' = -\mathbf{v}'\cdot\nabla(T_o + \Theta). \tag{C.5}$$

This eigenvalue problem leads to a seventh-order equation for the eigenvalue.

Because we are looking for the largest local eigenvalue λ on the collocation points, we could approximate $\mathbf{f}$ as a local constant and replace ∇ by the local mesh size $\Delta\mathbf{h}^{-1}$. Then we may obtain the following eigenvalues that possess the largest magnitude,

$$\tilde{\lambda} = -\mathbf{v}\cdot\Delta\mathbf{h}^{-1} \pm \sqrt{(\mathbf{v}\cdot\Delta\mathbf{h}^{-1})^2 + 4\left[\frac{1}{R_o}(\mathbf{B}\cdot\Delta\mathbf{h}^{-1})^2 - \frac{R_{th}T_0'}{R_o}\right]}. \tag{C.6}$$

APPENDIX D: MAGNETIC TORQUE AND THE ANGULAR MOMENTUM

The angular momentum of the inner core and the mantle can be written as

$$M_i = L_{ij}\omega_j, \tag{D.1}$$

where L_{ij} is the tensor of the momentum inertia and ω_i is the angular velocity. In this paper we assume the spherically symmetric system,

$$L_{ij} = L\delta_{ij}, \tag{D.2}$$

where, in nondimensional form,

$$L^{(i)} = \frac{\rho^{(i)}}{\rho}\int_{r\le r_{io}}(x^2+y^2)\,dV = \frac{8\pi}{15}\left(\frac{\rho^{(i)}}{\rho}\right)r_{io}^5, \tag{D.3}$$

$$L^{(m)} = \frac{\rho^{(m)}}{\rho}\int_{1\le r\le r_{eo}}(x^2+y^2)\,dV = \frac{8\pi}{15}\left(\frac{\rho^{(m)}}{\rho}\right)\left(r_{eo}^5 - 1\right). \tag{D.4}$$

The superscripts i and m in the above equations indicate the inner core and the mantle, respectively. Equations (D.2) and (D.3) are to leading order good approximations to the Earth because the Earth's ellipticity is small [41].

The magnetic torque on the inner core is, in nondimensional form,

$$\mathbf{\Gamma}_B = \Lambda\int_{r\le r_{io}}\mathbf{r}\times(\mathbf{J}\times\mathbf{B})\,dV = \Lambda\int_{r=r_{io}}(\mathbf{r}\times\mathbf{B})B_r\,dS. \tag{D.5}$$

Therefore,

$$\Gamma_{B,x} = \sqrt{\frac{2\pi}{3}}\Lambda\int_{r=r_{io}}\frac{r^2B_r}{\sin\theta}(rB_\phi\cos\theta - irB_\theta)Y_1^1\,d\Omega + \text{c.c.} \tag{D.6}$$

$$\Gamma_{B,y} = -\sqrt{\frac{2\pi}{3}}\Lambda\int_{r=r_{io}}\frac{r^2B_r}{\sin\theta}(rB_\theta + irB_\phi\cos\theta)Y_1^1\,d\Omega + \text{c.c.} \tag{D.7}$$

$$\Gamma_{B,z} = \sqrt{4\pi}\,\Lambda \int_{r=r_{io}} \left(r^2 B_r\right)(r B_\phi \sin\theta) Y_0^0 \, d\Omega, \tag{D.8}$$

where $d\Omega$ is the differential solid angle. Changing the signs in (D.6)–(D.8) and replacing $r = r_{io}$ by $r = 1$, we obtain the magnetic torque on the solid mantle.

The velocity field of a solid body rotation with the angular velocity $\boldsymbol{\omega}$ is of the form

$$\mathbf{v} = \boldsymbol{\omega} \times \mathbf{r} = (\omega_y z - \omega_z y)\mathbf{1}_x + (\omega_z x - \omega_x z)\mathbf{1}_y + (\omega_x y - \omega_y x)\mathbf{1}_z. \tag{D.9}$$

Applying the transform relations between the Cartesian coordinate and the spherical coordinate, we obtain

$$\begin{aligned}(r\sin\theta v_\theta) &= r^2(\omega_y \sin\theta\cos\phi - \omega_x \sin\theta\sin\phi)\\ &= -\sqrt{\frac{2\pi}{3}} r^2 \left[(\omega_y + i\omega_x) Y_1^1 + \text{c.c.}\right], \qquad \text{(D.10)}\\ (r\sin\theta\, v_\phi) &= \omega_z r^2 \sin^2\theta - r^2(\omega_x \sin\theta\cos\theta\cos\phi + \omega_y \sin\theta\cos\theta\sin\phi)\\ &= \omega_z r^2 \sin^2\theta + \sqrt{\frac{2\pi}{15}}\, r^2 \left[(\omega_x - i\omega_y) Y_2^1 + \text{c.c.}\right]. \qquad \text{(D.11)}\end{aligned}$$

The consequence of ignoring non-axisymmetric inertia is to eliminate fast, free precessions in our system. To demonstrate this, consider the horizontal torques

$$\Gamma_x = L A_x \sin\alpha t, \qquad \Gamma_y = L A_y \cos\alpha t. \tag{D.12}$$

By the full equation (2.10), we have

$$\omega_x = c_1 \sin\frac{t}{2R_o} + c_2 \cos\frac{t}{2R_o} + 2\frac{A_y + (2R_o\alpha)A_x}{1 - (2R_o\alpha)^2}\cos\alpha t \tag{D.13}$$

$$\omega_y = c_1 \cos\frac{t}{2R_o} + c_2 \sin\frac{t}{2R_o} - 2\frac{A_x + (2R_o\alpha)A_y}{1 - (2R_o\alpha)^2}\sin\alpha t, \tag{D.14}$$

where c_1 and c_2 are arbitrary constants that determine the free precessions. The free oscillations vary on a time scale of $1/(2R_o)$, or that of the rotation of the system. If the torques Γ_x and Γ_y vary on a much longer time, i.e., $\alpha \ll 1/(2R_o)$, then the approximation (2.23) determines to leading order the forced precessions that are described in the last terms in (D.13) and (D.14).

ACKNOWLEDGMENTS

We thank Drs. Glatzmaier and Roberts for many discussions about their work, Dr. Holme for providing eigenvalue results on benchmarking the Kumar–Roberts dynamo, and Drs. Bergman and St. Pierre for many useful discussions. This work was supported by the NSF under Grants EAR9317156 and EAR9526914, and by the Packard Foundation. W.K. is also supported by the NASA Solid Earth and Natural Hazard Program.

REFERENCES

1. G. A. Glatzmaier and P. H. Roberts, A three-dimensional convective dynamo solution with rotating and finitely conducting inner core and mantle, *Phys. Earth Planet. Inter.* **91**, 63 (1995).

2. G. A. Glatzmaier and P. H. Roberts, A three-dimensional self-consistent computer simulation of a geomagnetic field reversal, *Nature* **377**, 203 (1995).
3. G. A. Glatzmaier and P. H. Roberts, An anelastic evolutionary geodynamo simulation driven by compositional and thermal convection, *Phys. D* **97**, 81 (1996).
4. G. A. Glatzmaier and P. H. Roberts, Rotation and magnetism of Earth's inner core, *Science* **274**, 1887 (1996).
5. S. Kumar and P. H. Roberts, A three dimensional kinematic dynamo, *Proc. Roy. Soc. London Ser. A* **314**, 235 (1975).
6. S. Chandrasekhar, *Hydrodynamic and Hydromagnetic Stability* (Dover, New York, 1981).
7. T. G. Cowling, The magnetic field of sunspots, *Mon. Not. Roy. Astron. Soc*. **94**, 39 (1934).
8. D. Gubbins and P. H. Roberts, Magnetohydrodynamics of the Earth's core, in *Geomagnetism*, edited by J. A. Jacobs (Academic Press, London, 1987), Vol. 2, Chap. 1.
9. M. G. St. Pierre, *On the Numercial Simulation of Rapidly Rotating, Strong Field Dynamos*, Ph.D. thesis, 1993.
10. C. A. Jones, A. W. Longbottom, and R. Hollerbach, A self-consistent convection driven geodynamo model using a mean field approximation, *Phys. Earth Planet. Inter.* **92**, 119 (1995).
11. J. B. Taylor, The magnetohydrodynamics of a rotating fluid and the Earth's dynamo problem, *Proc. Roy. Soc. London. Ser. A* **274**, 274 (1963).
12. H. Goldstein, *Classical Mechanics* (Addison–Wesley, Reading, MA, 1980).
13. M. R. Walker, C. F. Barenghi, and C. A. Jones, A note on dynamo action at asymptotically small Ekman number, *Geophys. Astrophys. Fluid Dynam*. **88**, 261 (1998).
14. H. P. Greenspan, *The Theory of Rotating Fluids* (Cambridge Univ. Press, Cambridge, UK, 1968).
15. D. R. Fearn, M. R. E. Proctor, and C. C. Sellar, Nonlinear magnetoconvection in a rapidly rotating sphere and taylor's constraint, *Geophys. Astrophys. Fluid Dynam*. **77**, 111 (1994).
16. D. R. Fearn and M. R. E. Proctor, Magnetostrophic balance in non-axisymmetric, non-standard dynamo models, *Geophys. Astrophys. Fluid Dynam*. **67**, 117 (1992).
17. J. G. Tough and P. H. Roberts, Nearly symmetric hydrodynamic dynamos, *Phys. Earth Planet. Inter*. **1**, 288 (1968).
18. S. I. Braginsky, Nearly axially symmetric model of the hydromagnetic dynamo of the earth, *Geomag. Aeron*. **18**, 225 (1978).
19. D. Jault and J.-L. LeMouël, The topographic torque associated with a tangentially geostrophic motion at the core surface and inferences on the flow inside the core, *Geophys. Astrophys. Fluid Dynam*. **48**, 273 (1989).
20. J. Bloxham and A. Jackson, Time-dependent mapping of the magnetic field at the core-mantle boundary, *J. Geophys. Res*. **97**, 19537 (1992).
21. P. H. Roberts and K. Stewartson, On double-roll convection in a rotating magnetic system, J. *Fluid Mech*. **68**, 447 (1975).
22. D. Jault, Model *z* by computation and *t*aylor's condition, *Geophys. Astrophys. Fluid Dynam*. **79**, 99 (1995).
23. L. D. Landau and E. M. Lifshitz, *Fluid Mechanics* (Pergamon Elmsford, New York, 1981).
24. G. A. Glatzmaier, Numerical simulations of stellar convective dynamos. I. The model and method, *J. Comput. Phys*. **55**, 461 (1984).
25. C. Canuto, M. Y. Hussaini, T. A. Zang, and A. Quarteroni, *Spectral Methods in Fluid Dynamics* (Springer-Verlag, Berlin/New York, 1988).
26. B. K. Alpert and V. Rokhlin, A fast algorithm for the evaluation of legendre expansions, *SIAM J. Sci. Statist. Comput*. **12**, 158 (1991).
27. G. Dahlquist, A special stability problem for linear multistep methods, *BIT* **3**, 27 (1963).
28. C. W. Gear, *Numerical Initial Value Problems in Odrdinary Differential Equations* (Prentice Hall, New York, 1971).
29. F. H. Busse, Thermal instabilities in rapidly rotating systems, *J. Fluid Mech.* **44**, 441 (1970).
30. Jun-Ichi Yano, Asymptotic theory of thermal convection in rapidly rotating systems, *J. Fluid Mech*. **243**, 103 (1992).
31. G. R. Sarson and D. Gubbins, Three-dimensional kinematic dynamos dominated by strong differential rotation, *J. Fluid Mech*. **306**, 223 (1996).

32. R. Holme, Three-dimensional kinematic dynamos with equatorial symmetry: Application to the magnetic fields of uranus and neptune, *Phys. Earth Planet. Inter*. **102**, 105 (1997).
33. S. Childress and A. M. Soward, Convection-driven hydromagnetic dynamo, *Phys. Rev. Lett*. **29**, 837 (1972).
34. P. H. Roberts and D. Gubbins, Origin of the main field: Kinematics, in *Geomagnetism*, edited by J. A. Jacobs (Academic Press, London, 1987), Vol. 2, Chap. 2.
35. F. H. Busse, A model of the geodynamo, *Geophys. J. Roy. Astron. Soc*. **42**, 437 (1975).
36. P. A. Gilman and J. Miller, Numerical simulations of stellar convective dynamos. I. The model and method, *Astrophys. J. Suppl*. **46**, 211 (1981).
37. R. Hollerbach and C. A. Jones, Influence of the Earth's inner core on geomagnetic fluctuations and reversals, *Nature* **365**, 541 (1993).
38. J. Bloxham, Global magnetic field, in *Global Earth Physics* (AGU Reference Shelf, 1995), Vol. 1, pp. 47–65.
39. W. Kuang and J. Bloxham, A numerical model of the generation of the Earth's magnetic field, *Nature* **365**, 371 (1997).
40. S. I. Braginsky, Torsional magnetohydrodynamic vibrations in the Earth's core and variations in day length, *Geomag. Aeron*. **10**, 1 (1976).
41. F. D. Stacey, *Physics of the Earth* (Brookfield Press, 1992).